CrossMark

Hydrothermal synthesis of NiFe$_2$O$_4$ nano-particles: structural, morphological, optical, electrical and magnetic properties

K CHANDRA BABU NAIDU and W MADHURI*

Ceramic Composites Laboratory, Centre for Crystal Growth, VIT University, Vellore 632014, India

Abstract. NiFe$_2$O$_4$ nano-crystallites with an average diameter of 8.9 nm are synthesized via hydrothermal method. The single-phase spinel structure is confirmed from X-ray diffractograms. Morphology is analysed by transmission and field emission scanning electron microscopes. High specific surface area of 55.7 m^2 g^{-1} is obtained for nano-particles. The M–H loop and M–T curve behaviours are investigated by vibrating sample magnetometry. The optical band gap energy is estimated from the UV–visible spectrum. In addition, the frequency dependence of dielectric properties is investigated. Cole–Cole plots are drawn to study electrical conduction mechanism and the kind of relaxation—Debye or non-Debye type. Low a.c. conductivity and low magnetic losses are noticed at 5 MHz frequency, which are suitable for microwave device applications.

Keywords. Nano-materials; transmission electron microscope; dielectric constant; permeability; magnetic properties.

1. Introduction

Nano-ferrites are promising materials for microwave devices, magnetic resonance imaging (MRI), catalysis, magnetic recording, microwave absorbers, biosensors, biomedical drug delivery, power transformers and telecommunication applications, due to their high thermal stability and enhanced electrical, optical and magnetic properties when compared with bulk materials [1–4]. Nano-nickel-ferrite is a mixed spinel ferrite having cation distribution of [Ni^{2+}Fe^{3+}]$_A$[Ni^{2+}Fe^{3+}]$_B$ [5]. Many researchers have successfully synthesized NiFe$_2$O$_4$ nano-particles by various techniques such as co-precipitation [6], green nano-technology [7], sol–gel [8], reactive milling [9], solvothermal [10] and egg-white precursor [11] methods in order to investigate the structural, optical, morphological, electrical and magnetic properties. However, the hydrothermal method offers many advantages over the other methods such as low cost for sample preparation, high crystallinity, simplicity and usage of low temperatures. In this investigation, additionally, dielectric properties, impedance spectroscopic analysis and magnetic permeability properties are explored for as-synthesized nano-particles, which have not been reported earlier by the hydrothermal technique.

2. Experimental

In order to synthesize NiFe$_2$O$_4$ nano-particles, Ni(NO$_3$)$_2$· 6H$_2$O, Fe(NO$_3$)$_3$·9H$_2$O (each of 99.8% purity, Sigma Aldrich) and NaOH are taken as precursors. Deionized water

is used as a solvent. Nickel and iron nitrates are dissolved in distilled water by maintaining the ratio of nitrates (g):water (ml) as 1:3. The resultant solution is stirred until it gets converted into nano-particles. NaOH (g) is added little by little to the solution (ml) in 1:4 (NaOH:nitrates) ratio. The pH of 11 is maintained in the mixture to achieve pure spinel phases. Furthermore, the mixture is vigorously stirred for 2 h and transferred into a 300 ml Teflon-lined steel autoclave. The sealed autoclave is heat treated at 150°C for 48 h. After 48 h the autoclave is slowly cooled to room temperature (RT). The precursor in the autoclave is filtered and washed with acetone and distilled water many times till pH is decreased to 7. Later, nickel ferrite (NF) nano-particles are separated from the autoclave and dried at 60°C for 6 h. The synthesis part is depicted in figure 1. The as-prepared powder is characterized using an X-ray diffractometer (Bruker X-Ray Powder Diffraction Meter, Cu$_{K\alpha}$, λ = 0.15418 nm), a Field-emission Scanning Electron Microscope (Ultra 55 FE-SEM Carl Zeiss), a Transmission Electron Microscopy (TEM: Model Tecnai G20, FEI, USA), a JASCO UV–visible spectrophotometer (V-670 PC), an FT-IR spectrophotometer (IR affinity-1, Shimadzu), a HIOKI 3532-50 LCR controller (Japan) and a Vibrating Sample Magnetometer (EV-7 VSM with maximum applied field of +15 kOe) for structural, morpho logical, optical, electrical and magnetic properties, respectively.

3. Results and discussion

3.1 *Structural analysis*

Figure 2a depicts the variation of intensity as a function of two-theta angle (2θ) from 10° to 80° for NiFe$_2$O$_4$

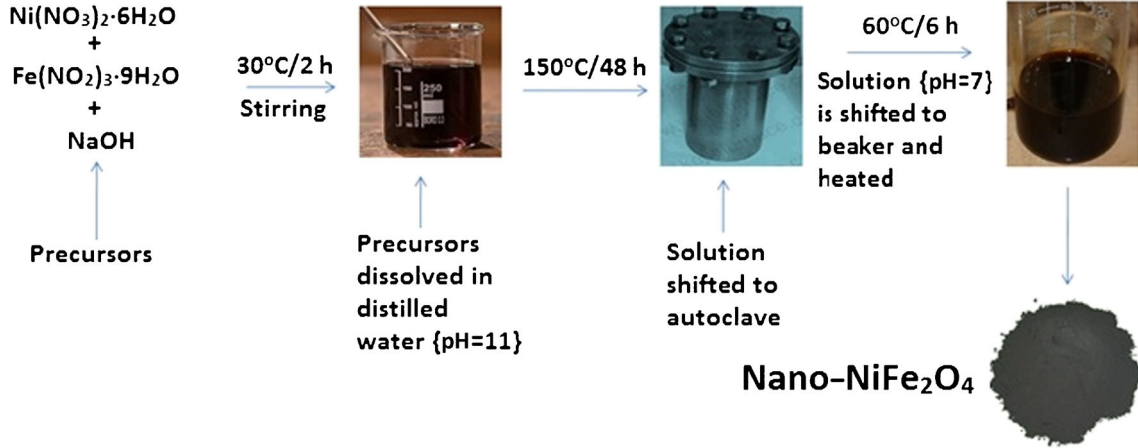*Author for correspondence (madhuriw12@gmail.com)

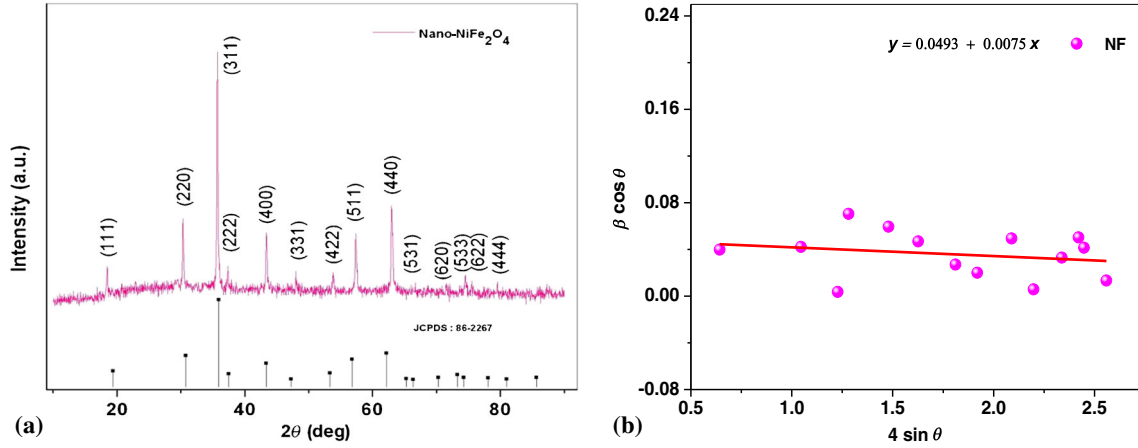**Figure 1.** Schematic diagram of synthesis part of nano-NiFe$_2$O$_4$.

Figure 2. (**a**) XRD pattern and (**b**) W–H plot of NiFe$_2$O$_4$ nano-particles.

nano-particles. The diffractogram pattern of as-prepared sample exhibited single-phase formation of face-centred cubic structure with high crystallinity. The locations of Bragg lines with reflections from the planes of (111), (220), (311), (222), (400), (422), (511), (440), (620), (533), (622) and (444) are in good agreement with standard JCPDS: 86-2267. The locations of main peaks are used to find inter-planar spacing (d) of Bragg's lines. No secondary phases are noticed in X-ray analysis. Thus, the obtained NF nano-particles are highly pure in phase. The average crystallite size 'D' (8.9 nm) is determined from average full-width at half-maxima (FWHM) of all reflection peaks using the Debye–Scherrer formula [12]:

$$D = \frac{0.9\lambda}{\beta \cos \theta}, \tag{1}$$

where β is FWHM, λ is wavelength of Cu$_{K\alpha}$ source (0.1542 nm) and θ is diffraction angle. The Williamson–Hall (W–H) plot (as shown in figure 2b) is drawn for $\beta \cos \theta$ *vs.* 4 sin θ in order to evaluate micro-strain (ε) and crystallite size (D) using the following relation [13]:

$$\beta \cos \theta = \frac{0.9\lambda}{D} + 4\varepsilon \sin \theta, \tag{2}$$

where slope of the straight line offers micro-strain while crystallite size is associated with the intercept parameter. This gives the correlation between 'ε' and 'D' values. The results are presented in table 1. The lattice constants (a, b and c) are computed from inter-planar spacing and Miller indices (h, k and l). The achieved value of 'a' (0.833 nm) is almost equal to the reported data [13]. X-ray density (5.393 g cm^{-3}) of nano-particles is calculated from the relation $D_x = ZM/Na^3$, where 'Z' is the number of molecules per unit cell ($Z = 8$), 'M' is the molecular weight of the composition, 'N' is Avogadro's number (6.023×10^{23}) and 'a' is the lattice parameter. Moreover, some structural parameters such as Scherrer strain (ε^*) and dislocation density (ρ_d) are calculated using the following relations [14] and are presented in table 1:

$$\varepsilon^* = \frac{\beta}{4 \tan \theta}, \tag{3}$$

$$\rho_d = \frac{1}{D^2}. \tag{4}$$

3.2 *Surface morphology*

Figure 3a shows the TEM images of NF nano-particles. The average particle size (D') of prepared sample is about 20 nm.

The obtained NF particle size is much smaller than the value 170 nm reported by Wang *et al* [15] via solvothermal technique (180°C/48 h). The reduction of particle size is attributed to lowering of the annealing temperature in the hydrothermal method (150°C/48 h). The surface area (*S*) is a physical property of nano-materials. This gets more importance than its bulk counterpart due to nano-ordered grain size. Basically, nano-materials will have large '*S*' value, whereas bulk materials will have small value. Magnetic properties of ferrites are very sensitive to the surface area [16]. The surface area obtained for the present nano-ferrite, 55.7 m^2 g^{-1}, is very large as calculated from TEM studies using the following relation:

$$S = \frac{6}{D'\rho_x}. \tag{5}$$

The magnetic interaction between nano-particles is responsible for the weak agglomeration in TEM photographs [16]. The selected area electron diffraction (SAED) indicates the good crystalline nature of single-phase nano-NiFe$_2$O$_4$ (figure 3b). The SAED pattern is indexed by (311), (400), (511) and (440) planes and is in agreement with diffraction data. The FE-SEM photographs and EDS spectra, including compositional data of as-synthesized NiFe$_2$O$_4$ powder

Table 1. Data on structural parameters of nano-NiFe$_2$O$_4$.

Parameters	Values	Literature	Reference
D' (nm)	20	46.2	2
a (Å)	8.327	8.332	2
$\rho_d \times 10^{14}$ (m^{-2})	126.2	—	—
FWHM (β_{avg})	0.023	—	—
D_x (g cm^{-3})	5.392	—	—
V	577.4	—	—
D (nm) from W–H plot	3.2	—	—
Scherrer strain ε^*	0.0156	—	—
Strain ε from W–H plot	0.0075	—	—
$S \times 10^3$ (m^2 g^{-1}) from TEM	55.67	—	—
Optical band gap, E_g (eV)	1.57	1.55	2

samples, are shown in figure 4. Diamond-cube-like grains are identified. Average grain size (G_a) is found to be of order 57.9 nm using the linear intercept method and is given by

$$G = \frac{1.5L}{MN}, \tag{6}$$

where *L* is the total test line length, *M* is the magnification and *N* is the total number of intercepts that the grain boundary makes with the line. EDS attributes the inhibited elements and impurities in the samples with their at% and wt%. No impurities are noticed in the EDS spectrum, once again confirming that the synthesized NF nano-particles are pure in nature.

3.3 *UV–visible spectra*

The diffuse reflectance spectrum is recorded in the range of 200–1500 nm for evaluating optical band gap of powder samples. The Kubelka–Munk function of reflectance *F*(*r*) is used to determine band gap [17]:

$$F(r) = \frac{(1-r)^2}{2r}. \tag{7}$$

The absorption coefficient (α) is directly proportional to *F*(*r*) and hence an equation to find band gap can be written as follows:

$$(\alpha h\nu)^n = m(h\nu - E_g), \tag{8}$$

where *m* is an energy-independent constant that depends on transition probability, E_g is optical band gap energy, *n* depends on the kind of transition, i.e., *n* = 2 for direct transition, 2/3 for direct forbidden transition, 1/2 for indirect transition and 1/3 for indirect forbidden transition, and *h*ν is photon energy [18]. In this study, *n* is taken as 2 for direct transition. E_g value is considered as the extrapolated tangent value towards *X*-axis for $(\alpha h\nu)^2$ *vs.* photon energy *h*ν (eV) plot as α tends to zero (figure 5). The band gaps of bulk (microwave sintered at 1000°C) and nano-NiFe$_2$O$_4$ (NF)
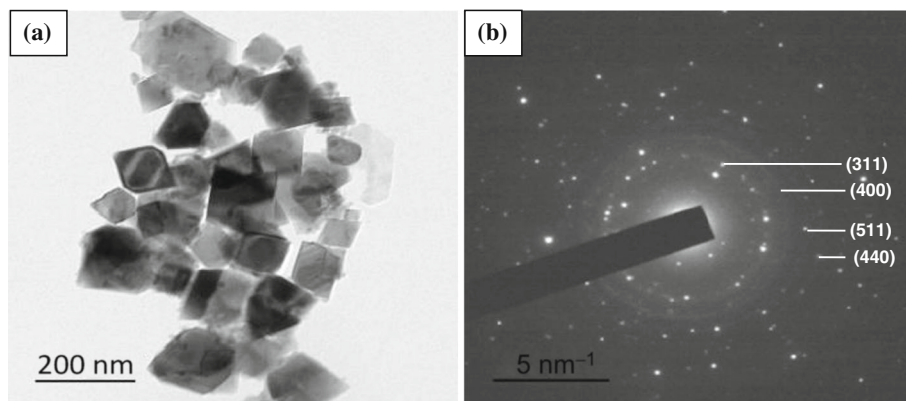

Figure 3. (a) TEM image and (b) SAED pattern of NiFe$_2$O$_4$ nano-particles.
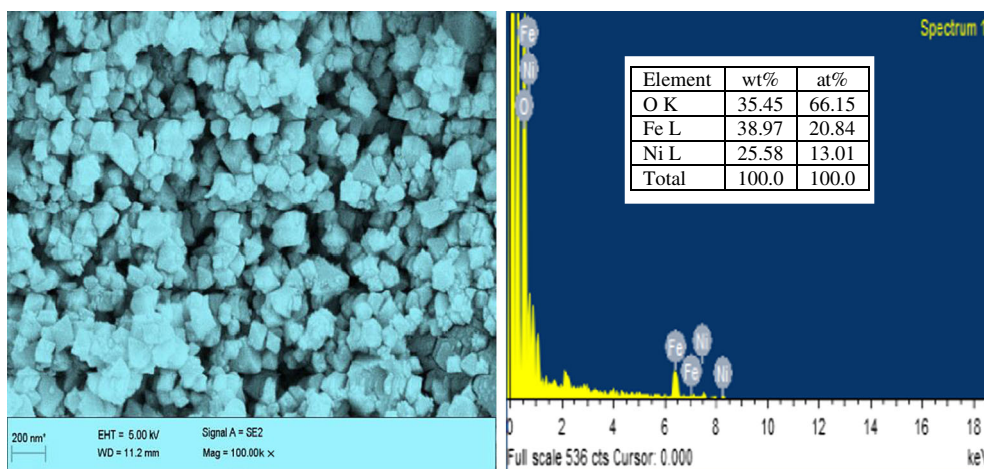
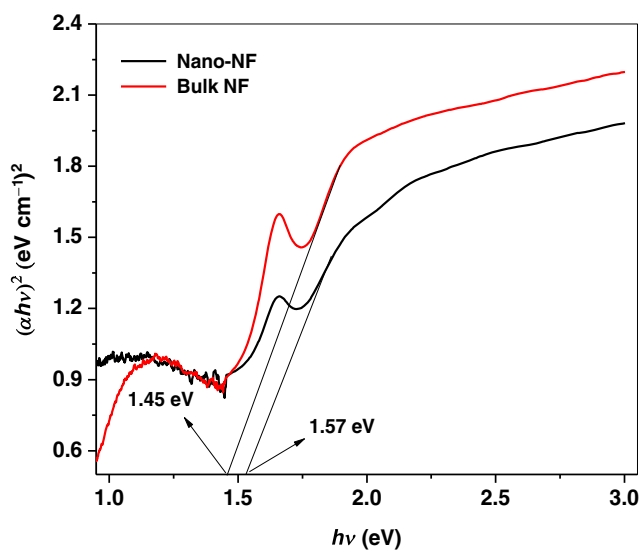**Figure 4.** FESEM image and EDS spectra of NiFe$_2$O$_4$ nano-particles.

Element	wt%	at%
O K	35.45	66.15
Fe L	38.97	20.84
Ni L	25.58	13.01
Total	100.0	100.0

Figure 5. Plot of $(\alpha h\nu)^2$ as a function of $h\nu$ (photon energy).

Figure 6. FT-IR spectra of NiFe$_2$O$_4$ nano-particles.

samples are calculated to be 1.45 and 1.57 eV, respectively. The obtained E_g of nano-NF is in consistent with the reported value of 1.56 eV [19]. Grain size variation and specific surface area are responsible for variation of band gaps of bulk ferrites and nano-ferrites. It is a known fact that the number of oxygen vacancies increases with decrease of grain size [19], i.e., nano-NFs (high surface area) possess more number of oxygen vacancies than their bulk (low surface area). Indeed, these oxygen vacancies act as electron (e$^-$) trapping centres and play a key role in reducing the recombination rate of photo-induced charge carriers (e$^-$ and h), intensifying photo-catalytic activity of ferrites [20]. However, more number of oxygen vacancies are created in nano-NiFe$_2$O$_4$, which are able to trap more number of carriers, leading to the reduction of electron–hole (e$^-$–h) separation efficiency. This enhances the photo-catalytic activity of nano-ferrite powders.
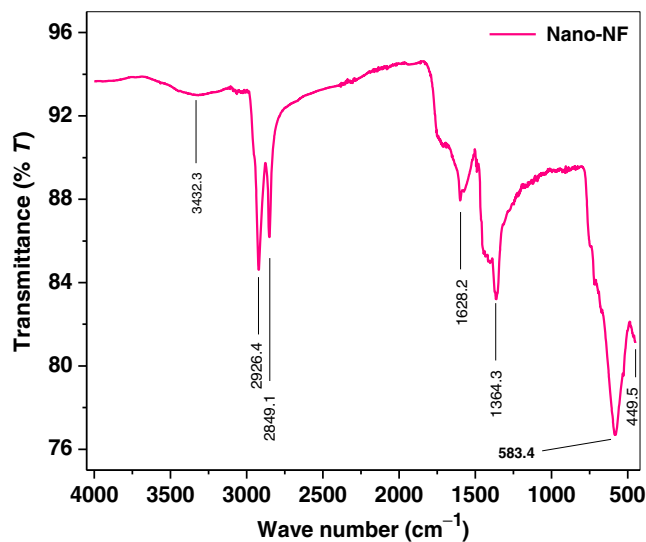
3.4 *FT-IR spectra*

FT-IR absorption spectrum in the range of 4000–400 cm^{-1} of as-prepared NiFe$_2$O$_4$ (NF) nano-particles is depicted in figure 6. Two kinds of metal-oxide (M-O) absorption bands are detected in the range of 400–590 cm^{-1}, confirming the formation of spinel NF. Bands at wave numbers 449.5, 583.4, 1364.3, 1628.2, 2849.1, 2926.4 and 3432.3 cm^{-1} appeared in the FTIR spectrum of nano-ferrite sample. The first and second absorption bands around 449.5 cm^{-1}(ν_1) and 583.4 cm^{-1}(ν_2) [21,22] are associated with metal oxide (Ni–O and Fe–O) stretching vibrations at octahedral B-site and Fe–O stretching vibrations at tetrahedral A-site, respectively [23]. The peak at 1364.3 cm^{-1} shows bending vibrations of O–H which are attributed to OH$^-$ absorbed by ferrites [22]. Some absorption bands that occur at 2849.1 and 2926.4 cm^{-1}
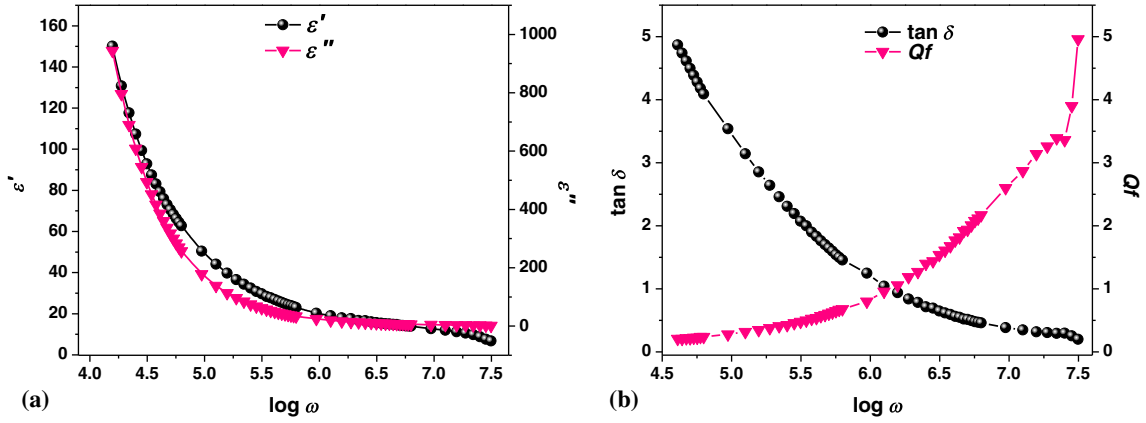
Figure 7. Variation of (**a**) real (ε') and imaginary (ε'') part of complex permittivity and (**b**) loss tangent (tan δ) and quality factor (Qf) with frequency.

are due to intra-molecular stretching modes that arise from different proportions of hydrogen bonding within the framework of tetrahedral bonded structure [24]. The detected bands at 1628.2 and 3432.3 cm^{-1} are due to O–H stretching and bending vibrations of H_2O molecules absorbed by nano-ferrites, respectively [22,23]. The force constants of both A-site ($K_t = 60.79$ N m^{-1}) and B-site ($K_o = 25.15$ N m^{-1}) are obtained by employing the Waldron method [25]. Mathematically, it is represented as

$$K_t = 7.62 M_t \nu_t^2 \times 10^{-7} (\text{N m}^{-1}), \tag{9}$$

$$K_o = 5.31 M_o \nu_o^2 \times 10^{-7} (\text{N m}^{-1}), \tag{10}$$

where M_t and M_o are the molecular weights of cations at tetrahedral and octahedral sites, respectively.

3.5 Electrical properties

The frequency dependence of real and imaginary parts of complex permittivity ($\varepsilon^* = \varepsilon' - j\varepsilon''$) is shown in figure 7a. The ε' and ε'' are referred to as dielectric constant and dielectric loss, respectively. It can be seen from figure 7a that ε' and ε'' achieve higher values at lower frequencies and decrease with increasing frequency. The Maxwell–Wagner interfacial polarization is responsible for high ε' and ε'' values at lower frequencies [26]. According to this theory, ferrimagnetic materials are assumed to have larger grains and smaller grain boundaries as conducting and insulating layers, respectively. Grain boundaries exhibit faster response to the input a.c. frequency at low frequencies, causing an increase in polarization. Hence, more number of ferrous (Fe^{2+}) ions are generated during the hopping mechanism, since hopping of carriers at the localized sites is universal in the Maxwell–Wagner double-layer model. Thus, ε', ε'' and tan δ (dissipation factor) values increase as shown in figure 7a and b. Moreover, grains are more active at high frequencies and lead to dielectric dispersion above certain critical frequencies. At these frequencies, the electron exchange oscillations between Fe^{3+}

Table 2. Data on electrical and permeability studies of nano-NiFe₂O₄.

Parameter	Value
ε' (5 MHz)	6.79
ε'' (5 MHz)	1.37
tan δ_e (5 MHz)	0.201
$\sigma_{a.c.}$ (S cm^{-1})	3.82×10^{-6}
$\sigma_{d.c.}$ (S cm^{-1})	1.29×10^{-6}
μ_i (5 MHz)	21.62
μ'' (5 MHz)	0.209
tan δ_M (5 MHz)	0.0097
tan δ_m/μ_i (5 MHz)	4.49×10^{-4}
Qf (5 MHz)	103

and Fe^{2+} ions cannot follow the applied a.c. frequency. This lowers the values of dielectric parameters at higher frequencies. Quality factor (Qf) is the reciprocal of loss tangent, and it increases with frequency. The slight knick observed in the loss tangent plot at higher frequencies must be due to the collective contribution of electrons and holes [27] at the interfacial boundary layer. In case of as-synthesized NF nano-particles, low dielectric constant and low losses are obtained at high frequencies due to high specific surface area (S) [28]. This high 'S' value is usually achieved owing to the small particle size (of nm range) of the sample. The values of a few dielectric parameters at 5 MHz frequency are given in table 2.

The frequency dependence of a.c. conductivity is shown in figure 8. It can be observed that the conductivity increases exponentially with increase of frequency up to 2.5 MHz. This happens due to sustained hopping of electrons between ferrous and ferric ions at octahedral sites [27]. After 4 MHz frequency a sharp drop-off of conductivity is noticed. This may be due to unavailability of ferrous ions at octal position, i.e., hopping rate of electrons is decreased [27]. At 5 MHz the a-chieved $\sigma_{a.c.}$ value is 3.82×10^{-6} S cm^{-1}, which is lower than the reported value (1.7×10^{-4}, $\sim 8 \times 10^{-6}$ and $\sim 1.25 \times 10^{-5}$ S cm^{-1})

for NF nano-crystallites prepared by egg-white precursor, citrate-gel and co-precipitation method, respectively [27–29].

The d.c. conductivity is evaluated from a power-law fit to the plot as per the following equation:

$$\sigma_{a.c.}(\omega, T) = \sigma_{d.c.}(T) + B\omega^n(\omega), \tag{11}$$

where $\sigma_{d.c.}$ is d.c. conductivity, B is a constant, n is the exponent and $\omega = 2\pi f$. In figure 8 the frequency-independent portion (between 2.5 and 4 MHz) is extrapolated towards Y-axis. Thus, the intersecting point establishes $\sigma_{d.c.}$ of 5.9×10^{-6} S cm^{-1}, whereas the exponent (n) value equals 0.156. The n value is in good agreement with that reported by the sol–gel auto-combustion method [30].

3.6 Impedance analysis

Impedance spectroscopic studies are useful for investigating the electrical properties of ferrites and will give information about grains and grain boundaries. In accordance with the Maxwell–Wagner double-layer model, the grains are considered to be high-conductance layers while grain boundaries are treated as low-conductance layers. Figure 9 depicts the Cole–Cole plot (Z' vs. Z'') of NiFe$_2$O$_4$ (NF) nano-particles at RT. The electron exchange between nickel and iron ions is responsible for the conduction mechanism in Nyquist plot. In this investigation the Cole–Cole plot shows two semicircular arcs within the complex plane. The first one is formed due to interfacial boundary (grain boundary) conduction at lower frequencies, while the latter is due the conduction through bulk crystals (grains) at high frequencies [31,32]. The centres of arcs lie below the real axis. Hence, it indicates the spread of relaxation with different (mean) time constants and confirms the non-Debye-type relaxation mechanism [32].
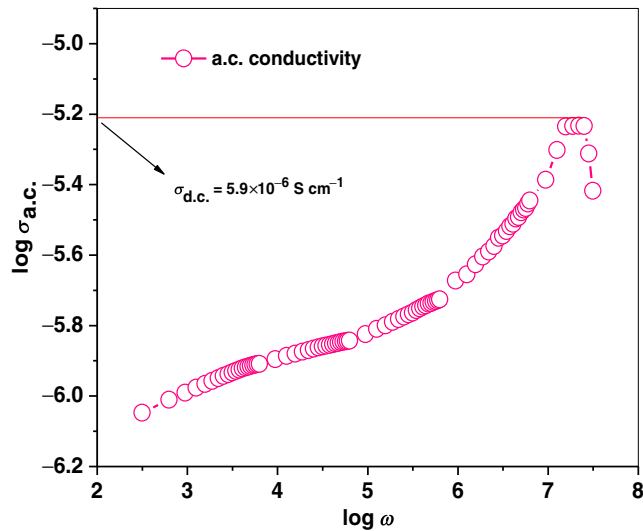
The obtained total bulk conductivity of NF is (1.29×10^{-6} S cm^{-1}) in agreement with d.c. conductivity value (3.82×10^{-6} S cm^{-1}) obtained from a.c. conductivity vs. frequency plot (figure 8). The values are higher than the reported value of 1.31×10^{-8} S cm^{-1} at RT [33]. Therefore, this result also confirms the semi-conducting nature of the material. This happens owing to the contribution of conductivities of grains and grain boundaries. The impedance is generally evaluated by an equivalent circuit of two parallel RC-elements connected in series. With the help of Z-view software, RC-elements are determined to be $R_1 = 0.13$ MΩ, $R_2 = 0.25$ MΩ, $C_1 = 5.09$ pF and $C_2 = 1.04$ nF. The corresponding relaxation times ($\tau_1 = R_1C_1$ and $\tau_2 = R_2C_2$) are evaluated. From the obtained results the relaxation time of grain ($\tau_1 = 0.65$ μs) is smaller than its boundary value ($\tau_2 = 256.5$ μs) since the semicircle of grain stays at higher frequencies while the interfacial boundary lies at lower frequencies (i.e., $\tau = 1/\omega$).

The complex electric modulus (M^*) is an indication of the extent of dielectric space-charge relaxation. The electric modulus is represented as $M^* = M' + jM''$ and can be calculated using the following relations:

$$M' = \frac{\varepsilon'}{\varepsilon'^2 + \varepsilon''^2}, \tag{12}$$

$$M'' = \frac{\varepsilon''}{\varepsilon'^2 + \varepsilon''^2}. \tag{13}$$

The RT electric modulus spectrum (M' vs. M'') is obtained from 50 Hz to 5 MHz frequency. In figure 10, two prominent semicircular arcs are noticed and the centres of arcs lie below the real axis. Hence, it is confirmed that the non-Debye-type dielectric relaxation is assigned to the present NF [32].
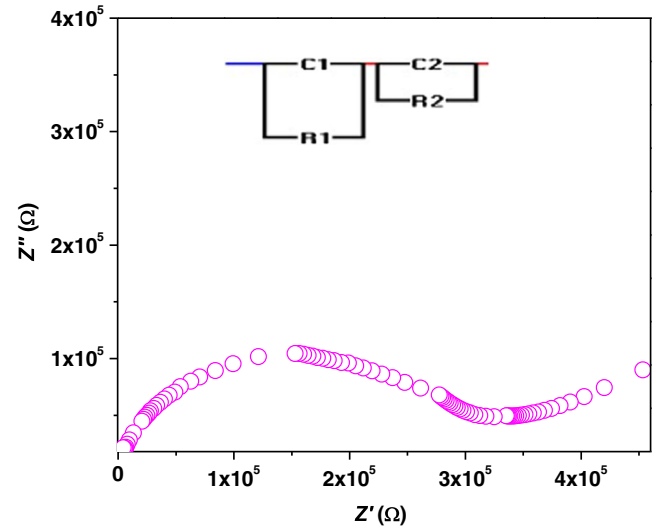
Figure 8. ln σ vs. frequency plot.

Figure 9. Z' vs. Z'' plot (Nyquist plot) of NiFe$_2$O$_4$ at room temperature.

3.7 *Magnetic properties*

Figure 11 shows the frequency dependence of initial permeability (μ') and magnetic loss (μ'') of toroidal shaped nano-NF. These are calculated using the following relation:

$$\mu' = \frac{L_s}{(0.004606N^2h \log 10(Do/Di))}, \qquad (14)$$

$$\mu'' = \mu' \tan\delta, \qquad (15)$$

where N is number of copper coil turns on the toroid (28 in this case), h is thickness of the toroid (inches), D_o, D_i are, respectively, outer and inner diameters (inches) and L_s is series inductance in μH [34]. It can be seen that the permeability increases with increase of frequency up to 0.4 MHz. For further increase of frequency, μ' decreases towards lower values due to resonance behaviour. As the applied field frequency matches with the precision frequency of dipoles, some amount of energy is propagated to the spinning dipoles
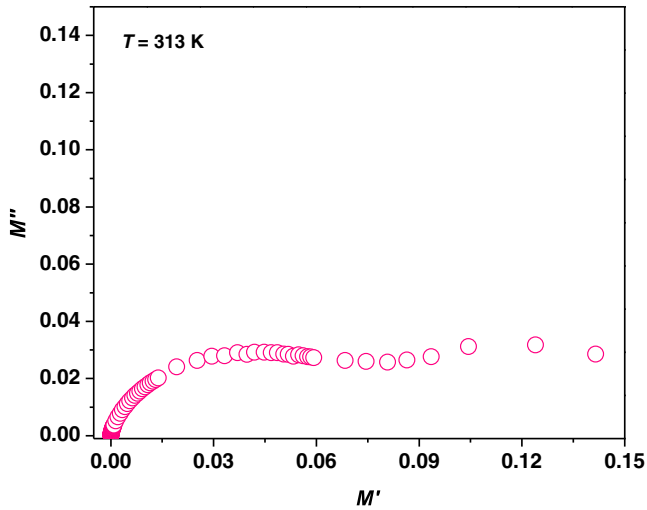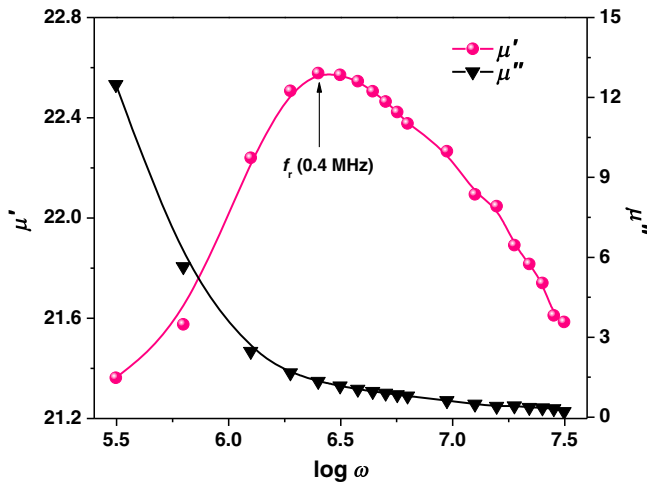
from input field. Therefore, μ' reaches the maximum value at resonance frequency (f_r). Above f_r, μ' obeys Snoek's law as $f_r \propto 1/(\mu'-1)$ [35]. The occurrence of ferromagnetic resonance peak is usual behaviour at higher frequencies [36]. On the other hand the magnetic loss (μ'') is generated due to the delay of magnetic dipoles in responding to the applied a.c. field frequency; μ'' decreases with increase of frequency. Low magnetic loss of 0.209 is obtained for NF at 5 MHz. Generally permeability is a grain-size-dependent property. Bulk materials possess particle size of micron order containing smaller number of oxygen vacancies. However, in case of nano-materials the number of oxygen ion vacancies is much greater, resulting in high pinning effect [37]. This pinning effect reduces the domain wall motion, leading to the decrease of permeability when compared with their bulk counterpart. Relative loss factor (rlf = $\tan\delta_m/\mu'$)
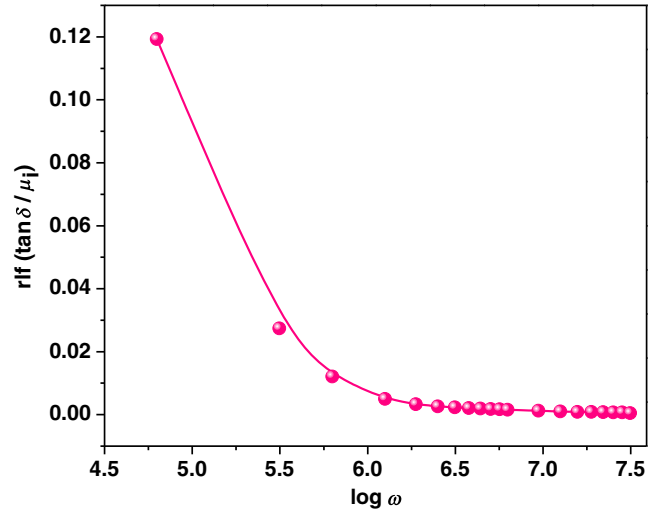

Figure 10. *M' vs. M'' plot at RT.*

Figure 11. Frequency dependence of real (μ') and imaginary (μ'') part of permeability at RT.

Figure 12. Frequency dependence of relative loss factor ($\tan\delta/\mu'$).

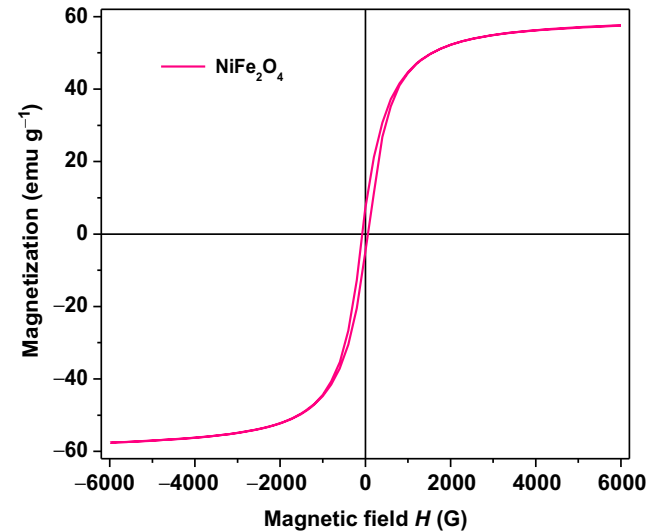**Figure 13.** *$M-H$ loop behaviour of NiFe$_2$O$_4$ nano-particles.*

is the ratio of magnetic loss tangent (tan δ_m) to permeability (figure 12). This must be as small as possible for device applications. In this study rlf decreases with increase of frequency and the lowest value achieved is of order 4.49×10^{-4} at 5 MHz. Permeability-related parameters' data are listed in table 2.

Magnetic properties of ferrites such as magnetization (M_s), remanence (M_r), coercivity (H_c), anisotropic energy ($K_1 \sim H_c M_s / 0.96$), squareness (M_r/M_s), M–H loop area (A) and magnetic moment (n_B) are affected by cationic distribution in the sites, surface area and density. The M–H loop (hysteresis loop) is traced for NF nano-particles at RT (300 K) and is shown in figure 13. The corresponding magnetic parameters are reported in table 3. As far as the cationic distribution of nano-NF is concerned, Ni^{2+} ions occupy B-site as well as A-site [5]; hence a few Fe^{3+} ions migrate from B-site to A-site. If M_A and M_B are the magnetic moments of tetrahedral and octahedral sites, respectively, the net magnetic moment ($M = M_B - M_A$) is equal to the experimental value of 2.417. Therefore the possible cationic distribution can be written as $[Ni_{0.205}Fe_{0.888}]_A$ $[Ni_{0.795}]_B[Fe_{1.112}]_BO_4$. In this study nano-NF exhibited more M_s of 57.6 emu g^{-1} and n_B of ($2.417\mu_B$) than the reported value using solvothermal technique [10] due to high specific surface area (low

Table 3. Data on M–H loop parameters of nano-NiFe$_2$O$_4$.

Parameter	Value	Literature	Reference
M_s (emu g^{-1})	57.6	54.8	10
A (cm^2)	1551.1	—	—
H_c (G)	65.1	59.4	10
M_r (emu g^{-1})	0.714	9.8	2
M_r/M_s	0.1024	—	—
K_1 (erg cm^{-2})	21061.2	—	—
n_B (μ_B)	2.417	—	—
ε_p (erg cm^{-2})	0.244	—	—
D_c (nm)	15.4	—	—

crystallite size) [1]. The critical diameter (D_c) is calculated from the following relation [38] and found to be 15.4 nm:

$$D_c = \frac{1.4\varepsilon_p}{M_s^2},\tag{16}$$

where $\varepsilon_p = (2K_bT_cK_1/a)^{1/2}$ is domain wall energy density, M_s is in Gauss, K_b is 1.38×10^{-16} erg K^{-1}, T_c (K) is the Curie temperature, K_1 is in erg cm^{-3} and a is lattice parameter (cm) [39]. The obtained D_c (15.4 nm) is of the order of crystallite diameter (D) of 8.9 nm. It is a well-known fact that if $D_c > D$ the generated H_c is the contribution of domain wall displacement. Likewise, if $D_c \sim D$, the coercivity is the result of domain-wall rotation [38]. Therefore, in this investigation the H_c, 65.1 G, is attributed to domain-wall rotation.

Figure 14a depicts the variation of magnetization as a function of temperature (M–T curve) of nano-NF. Zero-field-cooled (ZFC) magnetization measurements are carried out by cooling the NF in zero magnetic field and then the temperature is increased from 0 to 300 K under the applied field of 100 G. In the same way the field-cooled (FC) magnetizations are recorded by cooling NF from 300 to 0 K in 100 G static field. The ZFC curve shows the maximum magnetization ($\sim$40 emu g^{-1}) at around 260 K. This suggests the blocking of nano-particles at 260 K (T_B) [40]. For the temperature greater than blocking temperature ($T > T_B$, i.e., > 260 K) the magnetic moment of single-domain particles is progressively unblocked and the magnetization in the presence of magnetic field attains its thermal equilibrium value, like an atomic paramagnet. However, since the magnetic moment of a single-domain particle is larger than that of an atom, the magnetic state for $T > T_B$ is called super-paramagnetic, which exhibits almost zero values of coercivity and remanence of the material [41]. In this study, it happened at $T > 260$ K. The super-paramagnetic nature of nano-NF particles is very much clear from the M–H loop behaviour recorded at 270 K, wherein the coercivity and remanence
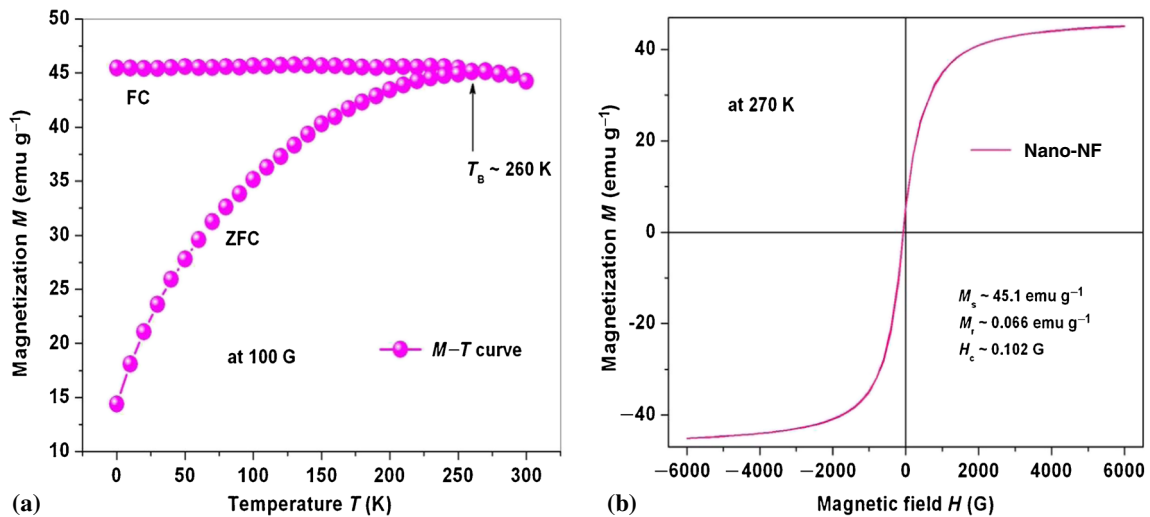

Figure 14. (a) M–T curve and (b) M–H loop (at 270 K) behaviour of NiFe$_2$O$_4$ nano-particles.

are almost equal to zero (figure 14b). At RT also the narrow M–H loop with almost zero M_r and very small H_c values confirms the existence of super-paramagnetic nature.

4. Conclusions

Nickel ferrite nano-particles are prepared by hydrothermal technique. The obtained crystallite size is 8.9 nm with good crystallinity. The SAED confirms the formation of nano-NiFe$_2$O$_4$ phases. Cole–Cole plots are drawn for complex impedance and dc-conductivity is found to be 1.29×10^{-6} S cm^{-1}. The as-prepared samples show high saturation magnetization of 57.6 emu g^{-1} and coercivity of 65.1 G. The M–T curve shows maximum magnetization $\sim$40 emu g^{-1} at blocking temperature T_B $\sim$260 K and for $T > T_B$ the NF shows super-paramagnetic nature. Low dielectric constant of 6.79 and low loss tangent of 0.201 are obtained at 5 MHz. The achieved low magnetic loss and low relative loss factor of 4.49×10^{-4} at 5 MHz are suitable for high-frequency magnetic applications.

References

[1] Mahmoud M H, Elshahawy A M, Makhlouf S A and Hamdeh H H 2014 *J. Magn. Magn. Mater.* **369** 55

[2] Rafique M Y, Ellahi M, Iqbal M Z, Javed Q and Pan L 2016 *Mater. Lett.* **162** 269

[3] Gabal M A, Kosa S and Al Mutairi T S 2014 *J. Mol. Struct.* **1063** 269

[4] Ranjith Kumar E, Jayaprakash R and Kumar S *J. Magn. Magn. Mater.* **351** 70

[5] Atif M, Nadeem M and Siddique M 2015 *Appl. Phys. A* **120** 571

[6] Luadthong C, Itthibenchapong V, Viriya-empikul N, Faungnawakij K, Pavasant P and Tanthapanichakoon W 2013 *Mater. Chem. Phys.* **143** 203

[7] Yehia M, Labib Sh and Ismail S M 2014 *Physica B* **446** 49

[8] Khairy M 2014 *Synth. Met.* **189** 34

[9] Marinca T F, Chicinas I, Isnard O, Pop V and Popa F 2011 *J. Alloys Compd.* **509** 7931

[10] Zheng H, Ni Y, Xiang N, Ma X and Wan F 2015 *Mater. Chem. Phys.* **158** 82

[11] Gabal M A, El-Shishtawy R M and Al Angari Y M 2012 *J. Magn. Magn. Mater.* **324** 2258

[12] Gabal M A and Al Angari Y M 2009 *Mater. Chem. Phys.* **118** 153

[13] Moradmard H, Shayeshtech S F, Tohidi P, Abbas Z and Khalegi M 2015 *J. Alloys Compd.* **650** 116

[14] Zaki H M, Al-Heniti S H and Elmosalami T A 2015 *J. Alloys Compd.* **633** 104

[15] Wang J, Ren F, Yi R, Yan A, Qiu G and Liu X 2009 *J. Alloys Compd.* **479** 791

[16] Mahmoud M H, Elshahawy A M, Makhlouf S A and Hamdeh H H 2014 *J. Magn. Magn. Mater.* **369** 55

[17] Koferstein R, Walther T, Hesse D and Ebbinghaus S G 2013 *J. Mater. Sci.* **48** 6509

[18] Chen W F, Chen H, Koshy P and Sorrell C C 2015 *J. Aust. Ceram. Soc.* **51** 1

[19] Dixit G, Singh J P, Srivastava R C, Agrawal H M and Chaudhary R J 2012 *Adv. Mater. Lett.* **3** 21

[20] Donnerberg H and Birkholz A 2000 *J. Condens. Matter Phys.* **12** 8239

[21] Moradmard H, Shayeshtech S F, Tohidi P, Abbas Z and Khalegi M 2015 *J. Alloys Compd.* **650** 116

[22] Dumitrescu A M, Lisa G, Iordan A R, Tudorache F, Petrila I, Borhan A I, Palamaru M N, Mihailescu C, Leontie L and Munteanu C 2015 *Mater. Chem. Phys.* **156** 170

[23] Sattara A A, El-Sayeda H M and Alsuqia I 2015 *J. Magn. Magn. Mater.* **395** 89

[24] Singh J P, Dixit G, Srivastava R C, Agrawal H M and Kumar R 2013 *J. Alloys Compd.* **551** 370

[25] Gabal M A, El-Shishtawy R M and Al Angari Y M 2012 *J. Magn. Magn. Mater.* **324** 2258

[26] Wagner K 1913 *Ann. Phys.* **40** 817

[27] Berchmens L J, Selvan R K, Kumar P N S and Augustin C O 2004 *J. Magn. Magn. Mater.* **279** 103

[28] Gabal M A, Al Angari Y M and Zaki H M 2014 *J. Magn. Magn. Mater.* **363** 6

[29] Varshney D and Verma K 2013 *Mater. Chem. Phys.* **140** 412

[30] Mocanu Z V, Airimioaei M, Ciomaga C E, Curecheriu L, Tudorache F, Tascu S *et al* 2014 *J. Mater. Sci.* **49** 3276

[31] Dzunuzovic A S, Ilic N I, Vijatovic Petrovic M M, Bobic J D, Stojadinovic B, Dohcevic-Mitrovic Z and Stojanovic B D 2015 *J. Magn. Magn. Mater.* **374** 245

[32] Ranjan R, Kumar N, Behera B and Choudhary R N P 2014 *Adv. Mater. Lett.* **5** 138

[33] Senthilkumar B, Kalai Selvan R, Vinothbabu P, Perelshtein I and Gedanken A 2011 *Mater. Chem. Phys.* **130** 285

[34] Ghodake J S, Shinde T J, Patil R P, Patil S B and Suryavanshi S S 2015 *J. Magn. Magn. Mater.* **378** 436

[35] Roy P K and Bera J 2012 *Mater. Chem. Phys.* **132** 354

[36] Stergiou C A and Litsardakis G 2016 *J. Magn. Magn. Mater.* **405** 54

[37] Song S, Song Q, Li J, Ramana M V and Zhang Z 2014 *Ceram. Int.* **40** 6473

[38] Caizer C 2015 *Handbook of nanoparticles* (Switzerland: Springer International Publishing) doi:10.1007/978-3-319-13188-7-24-1

[39] Caizer C and Stefanescu M 2003 *Physica B* **327** 129

[40] Dolia S N, Subhash Chander, Sharma M P and Sudhish Kumar 2006 *Indian J. Pure Appl. Phys.* **44** 169

[41] Atif M, Nadeem M and Siddique M 2015 *Appl. Phys. A* **120** 571